Int. J. Solids Structures, 1974, Vol. 10, pp. 709–734. Pergamon Press. Printed in Gt. Britain.

DYNAMIC PLASTIC DEFORMATION OF HEXAGONAL FRAMES†

CARL K. YOUNGDAHL

Components Technology Division, Argonne National Laboratory, 9700 South Cass Avenue, Argonne, Illinois 60439, U.S.A.

(*Received* 13 *August* 1973; *revised* 8 *November* 1973)

Abstract—The dynamic plastic response of a hexagonal frame to an internal pressure pulse of arbitrary shape is analyzed, including large-deformation geometric effects that result in redistribution of the bending and membrane reactions. Peak pressures of several multiples of the static yield load are considered, and the frame material is assumed to be rigid perfectly plastic. The effect of pulse shape on final plastic deformation is determined by numerically solving the governing sets of differential equations for a variety of parameter combinations. In the small deformation range, the permanent plastic deformation is shown to be dependent on an effective pressure, defined in terms of the first moment of the pressure pulse; the response duration is proportional to the pulse duration. In the large deformation range, the permanent plastic deformation is a function of the average pressure applied during the response, and the response duration depends on a characteristic time constant which is a function of material properties and hexagon size.

INTRODUCTION

A typical reactor core configuration consists of an array of long, thin-walled subassembly ducts of hexagonal cross section, each containing an array of fuel elements. The space between adjacent subassembly ducts is approximately equal to the wall thickness; this gap is maintained by spacer pads at various axial locations. Fuel replacement is accomplished by removal of a subassembly duct with its enclosed fuel elements by means of a fuel handling mechanism, which may be designed to extract only one subassembly at a time.

Fuel element failure may result in a fuel-coolant interaction or fission gas release which exposes the subassembly duct to an internal pressure pulse. The resulting duct deformation may be of the order of its wall thickness or larger, and plastic yielding of the wall may occur. If the permanent deformation is sufficiently large, the duct may be jammed into adjacent ducts or it may bind on the spacer pads during an attempt at removal of the damaged duct; then standard removal procedures may not be effective. If the damaged duct is adjacent to a control rod channel, interference with control rod motion may necessitate shutdown of the reactor until repairs can be made.

For a thin-walled, hexagonal crosssection, large-deformation geometric effects result in redistribution of the loading between the bending and membrane reactions, so that the deformed duct can withstand a static pressure higher than the yield limit of an undeformed hexagon. However, the application of a pressure pulse results in dynamic deformation, which may, because of inertia effects, significantly exceed the deformation caused by a static pressure having the same peak value. Conversely ,a pressure pulse may produce less deformation than a statically applied pressure if the duration of the pulse is sufficiently short.

† Work performed under the auspices of the U.S. Atomic Energy Commission.

Because of the statistical nature of the phenomena involved, pressure pulses resulting from fuel element failures are not well defined and are difficult to reproduce in laboratory simulations of pulse loadings on ducts. Accordingly, an analytical study has been performed to: develop a computational procedure for determining the dynamic plastic response of a hexagon to an internal pressure pulse, including large deformation effects; determine the effect of pulse shape on the permanent deformation of the hexagon; develop procedures for correlating permanent deformation with easily measured parameters associated with the pulse shape; and determine characteristic response times for plastic deformation of a thin-walled hexagon.

Results of the investigation indicate that in the small deformation range the final plastic deformation depends on the impulse and an effective pressure defined in terms of integrals of the pressure pulse, analogous to the correlation for other structural configurations[1]. The use of the impulse and effective pressure as correlation parameters eliminates the effect of pulse shape on final deformation and facilitates the interpretation of experimental results. The time scale of the dynamic deformation is proportional to the time scale of the pulse, as is typical of small-deformation plasticity solutions, and no intrinsic time constants are involved.

In the large deformation range, the final plastic deformation depends on the average pressure applied during the deformation. Characteristic time constants for the deformation were obtained in terms of material properties and hexagon dimensions; these are in the millisecond range for typical subassembly ducts, which corresponds to the time scale of pressure pulses resulting from fuel element failure.

The approach to the large-deformation analysis is similar to that used by Symonds and Mentel[2], Jones[3], and Symonds and Jones[4], for the finite plastic deflections of beams with axial restraints. The motion of the hexagon has an additional degree-of-freedom in that the corners of the hexagon are free to move along radial lines rather than being completely restrained as in the beam analyses. The "plastic string" phenomenon which appeared in the beam analyses did not occur here.

STATEMENT OF PROBLEM

A cross section of an internally pressurized hexagonal subassembly duct of wall thickness H and side width L is shown in Fig. 1. The effect of axial variation of the deflection shape is neglected compared with the geometric effects of large distortion of the cross section. Consequently, the problem is reduced to finding the dynamic plastic deformation of a hexagonal frame loaded by a time-dependent pressure $P(t)$. The redistribution of the dynamic loading between bending and membrane reactions as the deformation of the cross section proceeds is included in the analytical model for the large-deformation geometric effects. Because of symmetry, only the half-side AB need be considered.

The hexagon is assumed to be made of a rigid, perfectly plastic material having yield stress σ_y and density ρ. Elastic deformation is neglected compared with the plastic deformation; strain hardening is neglected compared with the large-deformation geometric effects.

Important constants of the hexagon deformation model include a geometric parameter α and a time constant t_0, defined by

$$\alpha = H/L,$$
$$t_0 = L\sqrt{\frac{\rho}{\sigma_y}}. \tag{1}$$

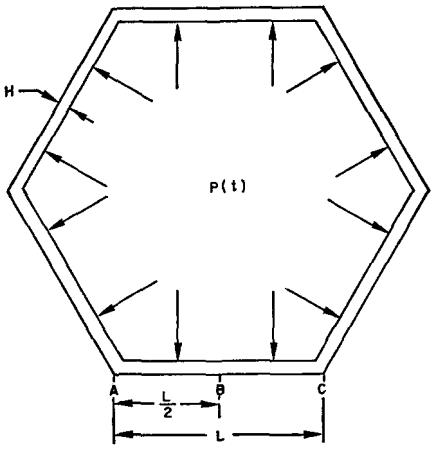

Fig. 1. Hexagon subjected to internal pressure pulse.

For an EBR-II reactor subassembly duct, $L = 1{\cdot}32$ in., $H = 0{\cdot}04$ in. and $\alpha = 0{\cdot}03$; for an FFTF reactor subassembly duct, $L = 2{\cdot}48$ in., $H = 0{\cdot}14$ in. and $\alpha = 0{\cdot}056$. These two duct sizes essentially span the range of typical duct designs. For steel ducts with a yield stress of 30,000 psi, $t_0 = 0{\cdot}16$ msec for EBR-II dimensions and $t_0 = 0{\cdot}3$ msec for FFTF dimensions.

Two variables of particular interest in this study are U_B, the outward deflection at the center of a side of the hexagon, and U_A, the outward deflection at a corner. A negative value for U_A, which occurs in some of the results shown here, indicates that the corners move inward. Another quantity of interest is the response duration t_f, i.e. the time interval over which dynamic plastic deformation occurs. The values of U_A and U_B at t_f will be denoted by U_{Af} and U_{Bf}, respectively.

Yield condition and flow rule

The yield condition, shown in Fig. 2, is given by

$$\frac{|M|}{M_0} + \frac{N^2}{N_0^2} - 1 = 0, \tag{2}$$

where N and M are, respectively, the resultant membrane force per unit axial length and bending moment per unit axial length arising from the stress distribution across the wall thickness at a plastically deforming location on the side of the hexagon; N_0 and M_0, the values of N and M for pure stretching and pure bending, are

$$N_0 = \sigma_y H, \qquad M_0 = \frac{\sigma_y H^2}{4}. \tag{3}$$

The plastic flow rule states that, during plastic flow, the generalized strain rate vector has the direction of the exterior normal to the yield condition at the considered generalized stress point[5]. Let Δ and θ be the stretch and angle change at a point on the side of the hexagon where plastic deformation is taking place. Then, writing equation (2) as $f(N, M) = 0$, we have

$$\frac{\mathrm{d}\Delta}{\mathrm{d}t} \Big/ \frac{\mathrm{d}\theta}{\mathrm{d}t} = \frac{\partial f}{\partial N} \Big/ \frac{\partial f}{\partial M}. \tag{4}$$

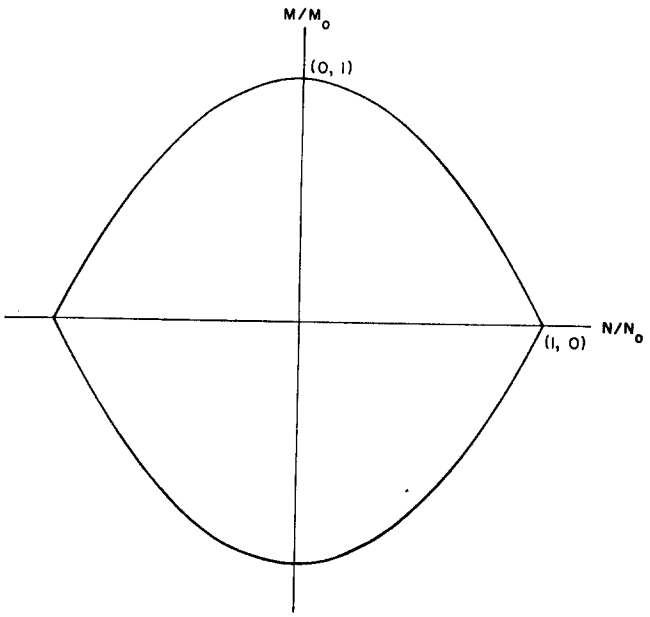

Fig. 2. Yield condition.

For the first quadrant of Fig. 2, which is the relevant one for this problem, the flow rule becomes

$$\frac{d\Delta}{dt} = \frac{N}{2\sigma_y}\frac{d\theta}{dt} \tag{5}$$

for $N < N_0$.

Limit load of undistorted hexagon

Let P_y be the limit load of the undistorted hexagon, i.e. the pressure at which the hexagon is in static equilibrium but plastic deformation is incipient. Plastic hinges are produced at the corners and centers of sides, where the yield condition is satisfied, and intermediate positions along the sides correspond to interior points of the yield condition (Fig. 2).

A free-body diagram of the half-side AB is shown in Fig. 3. From the equations of equilibrium in the horizontal direction, we have that the membrane forces at A and B are equal in magnitude (N_y) and opposite in direction. By equation (2), the bending moments at A and B must be equal in magnitude (M_y), and be directed as shown in Fig. 3 to resist the angle change. The symmetry of the problem requires that there be no vertical reaction at the midspan B and no reaction parallel to the dashed line at the corner A; this last condition implies that

$$N_y = \sqrt{3}F. \tag{6}$$

Equilibrium of moments and vertical forces requires that

$$M_y = \frac{P_y L^2}{16}, \qquad N_y = \frac{\sqrt{3}}{2}P_y L. \tag{7}$$

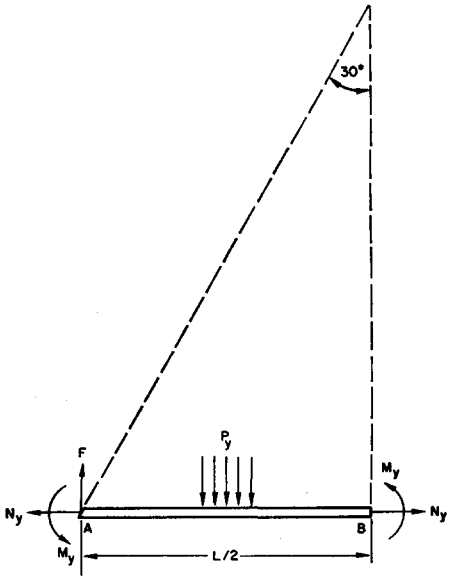

Fig. 3. Free-body diagram of hexagon half-side at initial yield.

Substitution from equations (7) into the yield condition (equation 2), results in a quadratic equation for P_y; its solution is

$$P_y = \frac{8\alpha^2\sigma_y}{1+\sqrt{1+48\alpha^2}}. \tag{8}$$

The bending moment distribution in the half-side is given by

$$M(x) = M_y\left(1-\frac{8x^2}{L^2}\right), \qquad 0 \le x \le \frac{L}{2} \tag{9}$$

where x is measured from point B. Consequently, the magnitude of M is equal to M_y at points A and B and less than M_y at interior points.

For $\sigma_y = 30{,}000$ psi, $P_y = 107$ psi for EBR-II duct proportions and $P_y = 363$ psi for FFTF duct proportions.

First plastic deformation mode

The simplest deformation mode which occurs during dynamic distortion has plastic hinges at the corners and midpoints of the sides of the hexagon connected by rigid sections of width $L/2$. A free-body diagram of the typical half-side AB is shown in Fig. 4. The stretches at the plastic hinges are Δ_A and Δ_B, and the angular rotation occurring at each hinge is θ. Because of symmetry, (1) the force resultants at A and B must be perpendicular to the dashed lines, and (2) the velocities and displacements of points A and B must be along the dashed lines. Therefore,

$$N_A = \sqrt{3}F \tag{10}$$

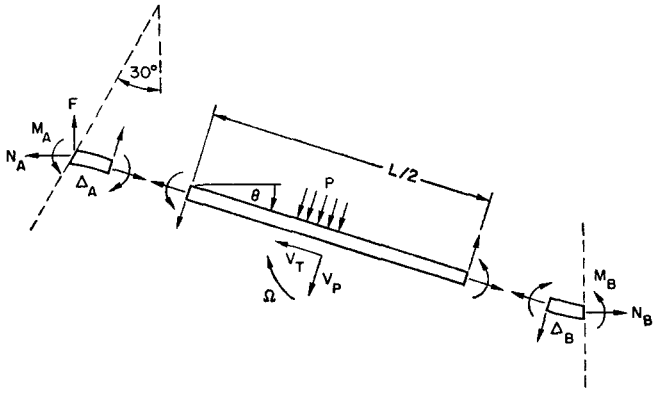

Fig. 4. Free-body diagram of hexagon half-side for first plastic-deformation mode.

and

$$\left[V_P + \left(\frac{L}{4} + \Delta_B\right)\Omega\right] \tan\theta = \frac{d\Delta_B}{dt} - V_T,$$
$$\left[V_P - \left(\frac{L}{4} + \Delta_A\right)\Omega\right] \tan\left(\frac{\pi}{6} - \theta\right) = \frac{d\Delta_A}{dt} + V_T, \tag{11}$$

where $\Omega(t)$ is the angular velocity, and $V_P(t)$ and $V_T(t)$ are the velocity components of the center of mass of the half-side perpendicular and parallel, respectively, to the instantaneous position of the half-side.

The equations of motion of the half-side of the hexagon are

$$\frac{\rho HL^3}{96}\frac{d\Omega}{dt} = -M_A - M_B - \frac{N_B L}{4}\sin\theta + \frac{N_A L}{4}\left(\frac{\cos\theta}{\sqrt{3}} - \sin\theta\right),$$
$$\frac{\rho HL}{2}\frac{dV_P}{dt} = \frac{PL}{2} - N_B\sin\theta + N_A\left(\sin\theta - \frac{\cos\theta}{\sqrt{3}}\right), \tag{12}$$
$$\frac{\rho HL}{2}\frac{dV_T}{dt} = N_A\left(\cos\theta + \frac{\sin\theta}{\sqrt{3}}\right) - N_B\cos\theta.$$

The yield condition and flow rule for the plastic hinges at A and B are

$$\frac{M_A}{M_0} + \left(\frac{N_A}{N_0}\right)^2 = 1, \qquad \frac{d\Delta_A}{dt} = \frac{N_A\Omega}{2\sigma_y},$$
$$\frac{M_B}{M_0} + \left(\frac{N_B}{N_0}\right)^2 = 1, \qquad \frac{d\Delta_B}{dt} = \frac{N_B\Omega}{2\sigma_y}. \tag{13}$$

The angular rotation θ is found from

$$\frac{d\theta}{dt} = \Omega, \tag{14}$$

and the displacements at the corner and midspan are given by

$$U_A = 2(\Delta_A + \Delta_B)\cos\theta - L(1 - \cos\theta),$$
$$U_B = \tfrac{1}{2}\sqrt{3}\,U_A + (\tfrac{1}{2}L + \Delta_A + \Delta_B)\sin\theta, \tag{15}$$

where U_A and U_B are measured positive outward along the dashed lines in Fig. 4.

Equations (10–15) give thirteen relations for determining the unknown functions of time N_A, N_B, M_A, M_B, F, Ω, V_P, V_T, Δ_A, Δ_B, θ, U_A, and U_B for a prescribed loading $P(t)$. This set of equations was solved numerically, using a computer subroutine based on the Bulirsch–Stoer extrapolation method for solving coupled ordinary differential equations[6].

The bending moment distribution in the vicinity of point B, the center of the side, is given by

$$M(x,t) = M_B + \frac{4x^2(4x - 3L)}{L^3}(M_A + M_B) + \frac{4x^2(x - L)}{L^2}N_B\sin\theta + \frac{2x^2(L - 2x)}{L^2}N_A\left(\frac{\cos\theta}{\sqrt{3}} - \sin\theta\right), \tag{16}$$

where x is measured from point B along the distorted side. The first derivative of M at B is zero. Therefore, the bending moment has a relative maximum at B if its second derivative there is negative. For some pulse shapes, the computed values of N_A, N_B, M_A, and M_B are such that the second derivative of M at B, given by

$$\left.\frac{\partial^2 M}{\partial x^2}\right|_{x=0} = -\frac{24}{L^2}(M_A + M_B) - \frac{8}{L}N_B\sin\theta + \frac{4}{L}N_A\left(\frac{\cos\theta}{\sqrt{3}} - \sin\theta\right), \tag{17}$$

becomes zero at some time while P is increasing. In order not to violate the yield condition at a point near B, which would occur if the second derivative changed sign, a hinge band begins to form at B and spreads out from there as P increases. Plastic deformation involving a hinge band at B and a hinge at A will be called the second plastic deformation mode and will be discussed next. By equation (17), the transition from the first to the second deformation mode is signaled by

$$-6(M_A + M_B) - 2N_B L\sin\theta + N_A L\left(\frac{\cos\theta}{\sqrt{3}} - \sin\theta\right) = 0. \tag{18}$$

Second plastic deformation mode

The second deformation mode has a plastic hinge at the corners and a hinge band at the center of each side; there are moving hinges at the ends of the hinge bands, and a rigid section of wall connects each moving hinge with the nearest corner hinge. A free-body diagram of the typical half-side AB is shown in Fig. 5. The half-width of the hinge band is $\varepsilon(t)L/2$, and the stretches at the moving hinge and corner hinge are Δ_ε and Δ_A, respectively.

As for the first mode, the symmetry of the problem requires that (1) the force resultants at A and B must be perpendicular to the dashed lines, and (2) the velocities V_A and V_B and the displacements U_A and U_B must be along the dashed lines. The condition on the force resultant at the corner gives

$$N_A = \sqrt{3}F, \tag{19}$$

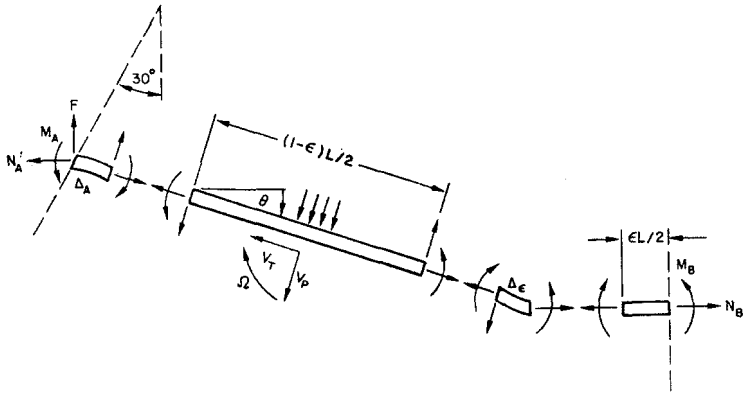

Fig. 5. Free-body diagram of hexagon half-side for second plastic-deformation mode.

and the condition on the velocity resultant at the corner gives

$$V_A \cos\frac{\pi}{6} = \left\{V_P - \left[\frac{L}{4}(1-\varepsilon) + \Delta_A\right]\Omega\right\}\cos\theta + \left[\frac{L}{4}\frac{d\varepsilon}{dt} - V_T - \frac{d\Delta_A}{dt}\right]\sin\theta,$$
$$\left\{V_P - \left[\frac{L}{4}(1-\varepsilon) + \Delta_A\right]\Omega\right\}\tan\left(\frac{\pi}{6} - \theta\right) + \left[\frac{L}{4}\frac{d\varepsilon}{dt} - V_T - \frac{d\Delta_A}{dt}\right] = 0. \tag{20}$$

Assuming that M and N do not vary along the hinge band, all plastic deformation associated with the band occurs at the moving hinge at its end. Since the velocity at B is vertical by the second symmetry condition above, the horizontal velocity component at the end of the band is the band growth rate $\frac{L}{2}\frac{d\varepsilon}{dt}$. Let the vertical velocity component at the end of the band be V_ε (positive downward); the velocity components at the end of the band are then related to motion of the rigid portion of the half-side through

$$\frac{L}{2}\frac{d\varepsilon}{dt} = \left\{V_P + \left[\frac{L}{4}(1-\varepsilon) + \Delta_B\right]\Omega\right\}\sin\theta + \left(\frac{L}{4}\frac{d\varepsilon}{dt} + V_T - \frac{d\Delta_B}{dt}\right)\cos\theta,$$
$$V_\varepsilon = \left\{V_P + \left[\frac{L}{4}(1-\varepsilon) + \Delta_B\right]\Omega\right\}\cos\theta - \left(\frac{L}{4}\frac{d\varepsilon}{dt} + V_T - \frac{d\Delta_B}{dt}\right)\sin\theta. \tag{21}$$

The equation of motion for the hinge band region is

$$\rho H \frac{dV(x,t)}{dt} = P(t), \qquad 0 \le x \le \frac{\varepsilon L}{2}; \tag{22}$$

this can be integrated to give

$$\rho H V(x,t) = \int P\,dt + G(x), \qquad 0 \le x \le \frac{\varepsilon L}{2}, \tag{23}$$

where $G(x)$ is a function to be determined from the motion. In particular, letting $x = 0$ gives

$$\rho H V_B = \int P\,dt + G(0), \tag{24}$$

and letting $x = \dfrac{\varepsilon L}{2}$ gives

$$\rho H V_\varepsilon = \int P \, dt + G\left(\frac{\varepsilon L}{2}\right). \tag{25}$$

The equations of motion of the rigid portion of the half-side are

$$\begin{aligned}
&\frac{\rho H L^3 (1-\varepsilon)^3}{96}\frac{d\Omega}{dt} = -M_A - M_B + \frac{L(1-\varepsilon)}{4}\left[-N_B \sin\theta + N_A\left(\frac{\cos\theta}{\sqrt{3}} - \sin\theta\right)\right],\\
&\frac{\rho H L(1-\varepsilon)}{2}\frac{dV_P}{dt} = \frac{PL(1-\varepsilon)}{2} - N_B \sin\theta - N_A\left(\frac{\cos\theta}{\sqrt{3}} - \sin\theta\right),\\
&\frac{\rho H L(1-\varepsilon)}{2}\frac{dV_T}{dt} = N_A\left(\cos\theta + \frac{\sin\theta}{\sqrt{3}}\right) - N_B \cos\theta.
\end{aligned} \tag{26}$$

The yield condition and flow rule for the plastic hinges at the corner and end of the hinge band are

$$\begin{aligned}
&\frac{M_A}{M_0} + \left(\frac{N_A}{N_0}\right)^2 = 1, \qquad \frac{d\Delta_A}{dt} = \frac{N_A \Omega}{2\sigma_y},\\
&\frac{M_B}{M_0} + \left(\frac{N_B}{N_0}\right)^2 = 1, \qquad \frac{d\Delta_\varepsilon}{dt} = \frac{N_B \Omega}{2\sigma_y}.
\end{aligned} \tag{27}$$

The angular rotation, displacement at the corner, and displacement at midspan are given by

$$\frac{d\theta}{dt} = \Omega, \qquad \frac{dU_A}{dt} = V_A, \qquad \frac{dU_B}{dt} = V_B, \tag{28}$$

where V_A and V_B are found from equations (20) and (24).

The bending movement distribution near the hinge band end of the rigid portion of the half-side is

$$\begin{aligned}
M = M_B + \left(x - \frac{\varepsilon L}{2}\right)^2 \Bigg\{ &\frac{4(4x + \varepsilon L - 3L)}{L^3(1-\varepsilon)^3}(M_A + M_B)\\
&+ \frac{2}{L^2(1-\varepsilon)^2}\left[(2x + \varepsilon L - 2L)N_B \sin\theta + (L - 2x)N_A\left(\frac{\cos\theta}{\sqrt{3}} - \sin\theta\right)\right]\Bigg\}.
\end{aligned} \tag{29}$$

The derivative $\partial M/\partial x$ is zero at $x = \varepsilon L/2$. Let

$$Q = \frac{\partial^2 M}{\partial x^2} \quad \text{at} \quad x = \frac{\varepsilon L}{2}. \tag{30}$$

The yield condition would be violated in the vicinity of the end of the band if Q were positive. If the hinge band is increasing in size, we have

$$Q = 0 \quad \text{for} \quad \frac{d\varepsilon}{dt} \geq 0 \tag{31}$$

and if it is decreasing in size,

$$Q < 0 \quad \text{for} \quad \frac{d\varepsilon}{dt} < 0. \tag{32}$$

Differentiating equation (29) twice and evaluating the result at $x = \varepsilon L/2$ gives

$$Q = -\frac{24}{L^2(1-\varepsilon)^2}(M_A + M_B) + \frac{4}{L(1-\varepsilon)}\left[-2N_B \sin\theta + N_A\left(\frac{\cos\theta}{\sqrt{3}} - \sin\theta\right)\right]. \tag{33}$$

For ε increasing (which occurs, in general, for P increasing), equations (12–21), (24–28), and (31) are eighteen relations for determining the unknown functions N_A, N_B, M_A, M_B, F, Ω, V_P, V_T, V_A, V_B, V_ε, Δ_A, Δ_ε, θ, U_A, U_B, ε, and G for a prescribed loading $P(t)$ such that the motion is in the second deformation mode. If the hinge band is decreasing in size, equation (31) does not apply; however, $G(x)$ is now a known function since ε is retreating through the same values it passed through as it was increasing. Consequently, there is one less unknown function, and one less equation is needed.

Other plastic deformation modes

The two deformation modes described above each result in the hexagon being distorted into an irregular twelve-sided figure. Severe loadings can produce transitions to higher deformation modes with twenty-four sides, forty-eight sides, and so on, until an approximately circular shape is attained. Such gross distortions of the cross section are beyond the scope of this study, and only the first and second deformation modes are treated.

Initial conditions

At the onset of plastic yielding, all velocities and deformations are zero. If the pressure passes gradually through the yield load, the initial conditions on the membrane forces and bending moments are given by equations (7).

An initial instantaneous jump to a pressure P_i can produce either first or second deformation mode response. For the first mode response, the initial condition on the membrane forces is determined by solving the simultaneous equations

$$\begin{aligned} &\frac{(N_A - N_B)}{N_B}\left[\frac{2\sqrt{3}\alpha(N_A + N_B)}{N_0} + 1\right] + \frac{2\alpha N_A}{\sqrt{3}N_0} = \frac{P_i}{\sigma_y}, \\ &\frac{N_A - N_B}{N_B} + 6\alpha^2\left(2 - \frac{N_A^2 + N_B^2}{N_0^2}\right) - 2\sqrt{3}\,\alpha\frac{N_A}{N_0} = 0. \end{aligned} \tag{34}$$

The initial condition on the bending moments is then found from equations (13).

For second mode response, the initial conditions on the membrane forces are

$$\begin{aligned} \frac{N_A}{N_0} &= (1 + C_1)C_2, \\ \frac{N_B}{N_0} &= (1 - C_1)C_2, \end{aligned} \tag{35}$$

and the initial hinge band width is

$$\varepsilon = 1 - \frac{\alpha(1 + C_1)C_2}{\sqrt{3}\,C_1}, \tag{36}$$

where C_1 and C_2 are defined by

$$C_1 = \frac{2\dfrac{P_i}{\sigma_y}}{4 - \dfrac{P_i}{\sigma_y} + \sqrt{\left(4 - \dfrac{P_i}{\sigma_y}\right)^2 + 112\dfrac{P_i}{\sigma_y}}},$$
$$C_2 = \left[\frac{9C_1}{9C_1(1 + C_1^2) + (1 + C_1)^2}\right]^{1/2}. \tag{37}$$

Again, the initial values of M_A and M_B are found from the yield condition.

Let P_h be the initial jump pressure which marks the transition between first and second mode response. This transition pressure can be determined either by finding the value of P_i such that the values of N_A, N_B, M_A, and M_B calculated from equations (13) and (34) satisfy equation (18) for $\theta = 0$ or by finding the value of P_i such that $\varepsilon = 0$ in equation (36). The result is

$$\frac{P_h}{\sigma_y} = \frac{4C(1 + 7C)}{1 + C}, \tag{38}$$

where C is related to α through

$$\alpha^2 = \frac{C}{3} + \frac{3C^2(1 + C^2)}{(1 + C)^2}. \tag{39}$$

For small values of α, P_h is approximately $3P_y$.

RESULTS

In order to illustrate some qualitative aspects of the hexagon response, results of two typical problems will be shown first†. Consider an exponential decay pulse of the form

$$P(t) = P_m e^{-t/t_1}, \qquad t \geq 0$$
$$P(t) = 0, \qquad t < 0. \tag{40}$$

Let $\alpha = 0{\cdot}056$; then $P_y = 0{\cdot}0121\,\sigma_y$ by equation (8). Take $P_m = 2P_y = 0{\cdot}0242\,\sigma_y$ for each problem, but let $t_1 = 0{\cdot}01\,t_0$ in the first example and $t_1 = 2t_0$ in the second, where t_0 is defined in equations (1). The dimensionless quantities P/σ_y, N_B/N_0, U_A/H, and U_B/H are shown in Figs. 6 and 7 as functions of time for each of the two examples.

Comparison of the results, which are for the same peak pressure but different pulse duration, indicates significant qualitative and quantitative differences in the responses. For the shorter duration pulse, the final permanent deformation at the center of the side is approximately $1{\cdot}88H \times 10^{-4}$, which is in the small deformation range; for the longer duration pulse, $U_B = 1{\cdot}61H$ at the end of the motion, which is in the large deformation range. The final deformations at the corners are $7{\cdot}6H \times 10^{-6}$ for $t_1 = 0{\cdot}01t_0$ and $-0{\cdot}25H$ for $t_1 = 2t_0$, the negative sign indicating that the corners move inwards. Thus the corner deflection is small compared to the mid-span deflection in the first example, but it is proportionately larger in the second. For the longer duration pulse, the corners move out initially

† See Ref. [7] for a more detailed presentation of results.

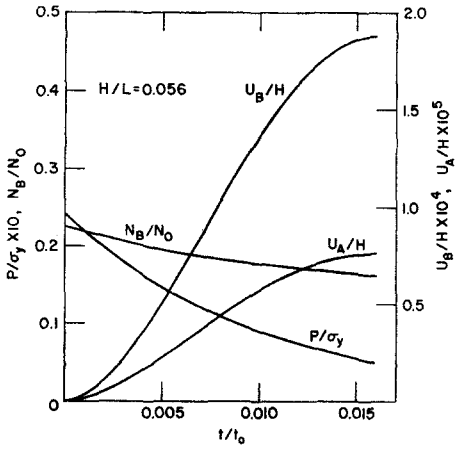

Fig. 6. Typical small deformation results.

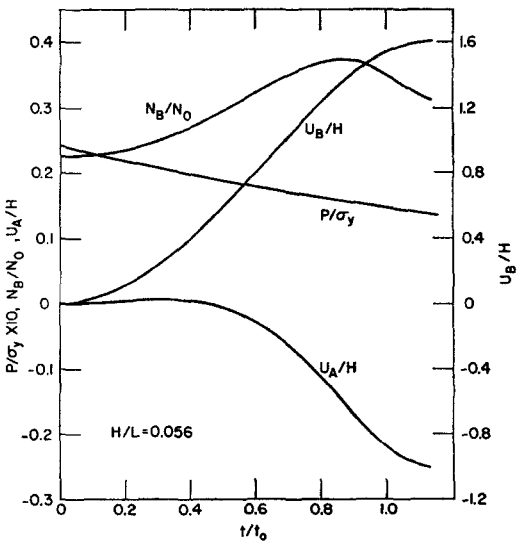

Fig. 7. Typical large deformation results.

and then later move in as the large-deformation membrane effects become more important; the motion stops at a time when the applied pressure is still greater than the yield pressure of the undeformed hexagon, which shows that the inclusion of the large deformation effects results in a strengthening of the hexagon.

Consider a rectangular pulse defined by

$$\begin{aligned} P(t) &= P_r, \qquad 0 \le t \le t_r, \\ P(t) &= 0, \qquad t < 0 \quad \text{and} \quad t > t_r. \end{aligned} \tag{41}$$

Figure 8 shows the final midspan deflection U_{Bf} and the response duration t_f as functions of the pulse duration t_r for $\alpha = 0{\cdot}056$ and $P_r = 2P_y$. In the small deformation range the curves for t_f/t_0 and U_{Bf}/H are straight lines with slopes of one and two, respectively, indicat-

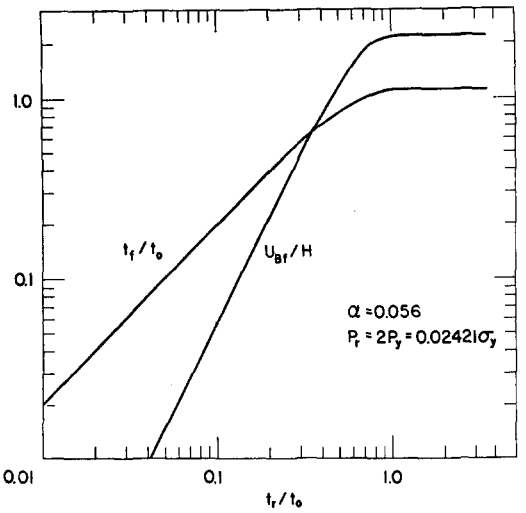

Fig. 8. Final midspan deflection and response duration as functions of rectangular pulse duration.

ing that t_f is directly proportional to t_r and U_{Bf} varies as t_r^2. As the pulse duration is increased, the final deflection and response duration increase until $t_r/t_0 = 1{\cdot}11$. For values of t_r greater than $1{\cdot}11t_0$, the deformation stops before the end of the pulse because the hexagon is distorted into a shape that can statically withstand the applied pressure†. Consequently the response to a step pulse is identical to the response to a rectangular pulse of the same magnitude if t_r is sufficiently large. The maximum midspan deflection is about 2·2 times the wall thickness for this combination of P_r and α.

Small deformation response

The dependence of the hexagon response in the small deformation range on the geometric parameter α is essentially only through the yield load P_y. This can be seen from Figs. 9 and 10 where $(U_{Bf}/H)(t_0/t_r)^2$ and t_f/t_r are plotted as functions of P_r/P_y for short duration rectangular pulses. The division of U_{Bf} by t_r^2 and t_f by t_r is suggested by the small deformation behavior exhibited in Fig. 8. The range of values of α shown in Figs. 9 and 10 exceeds the range of physically realistic subassembly duct designs.

The effect of pulse shape on permanent plastic deformation has been investigated for a variety of structural configurations[1]. The deformations were assumed to be small for each configuration, and each was assumed to be made of a rigid, perfectly plastic material. In each case it was found that the maximum permanent plastic deformation, U_f say, could be approximated by

$$U_f \approx I^2 f(P_e), \tag{42}$$

where f is a function, I is the impulse, and P_e is an effective value of the load. In essence, an arbitrary pulse can be replaced by an equivalent rectangular pulse of height P_e and duration t_e, where

$$\begin{aligned} P_e &= I/t_e, \\ t_e &= 2t_m. \end{aligned} \tag{43}$$

† Because of the kinetic energy involved in the dynamic deformation, the distortion overshoots the amount necessary to contain the applied pressure statically[8].

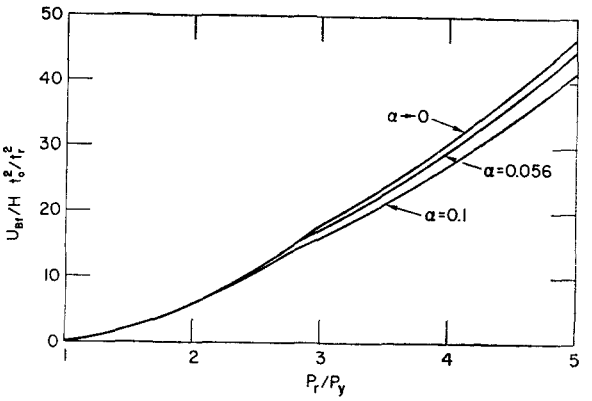

Fig. 9. Effect of α on final mid-span deflection in small deformation range.

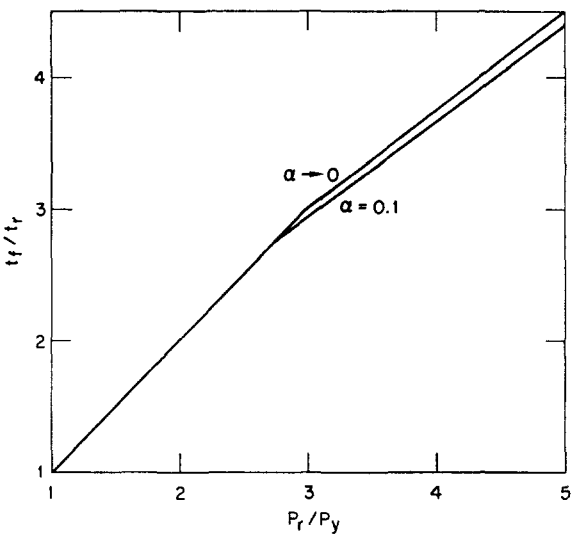

Fig. 10. Effect of α on response duration in small deformation range.

In the above, t_m is the mean time of the pulse measured from the time t_y when plastic deformation is initiated and I is the applied impulse during plastic deformation, i.e.

$$t_m = \frac{1}{I}\int_{t_y}^{t_f}(t - t_y)P(t)\,dt,$$
$$I = \int_{t_y}^{t_f} P(t)\,dt. \tag{44}$$

The final time t_f needed to evaluate the integrals in equations (44) can be computed approximately from

$$t_f - t_y \approx I/P_y. \tag{45}$$

The correlation indicated in equation (42) is valid also for small deformations of a hexagon. Figures 11 and 12 show U_{Bf}/I^2 (nondimensionalized) as a function of P_m/P_y and P_e/P_y,

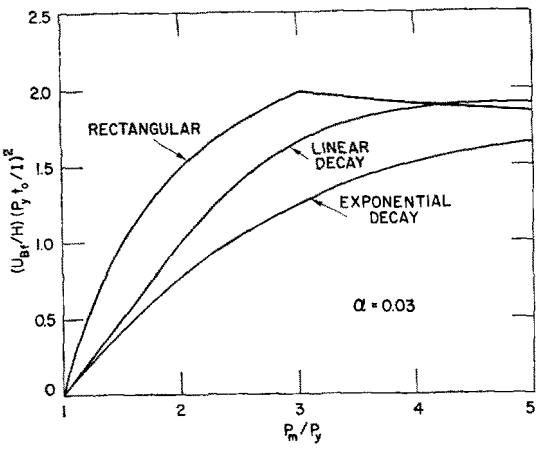

Fig. 11. Final mid-span deflection in small deformation range as function of peak pressure for various pulse shapes.

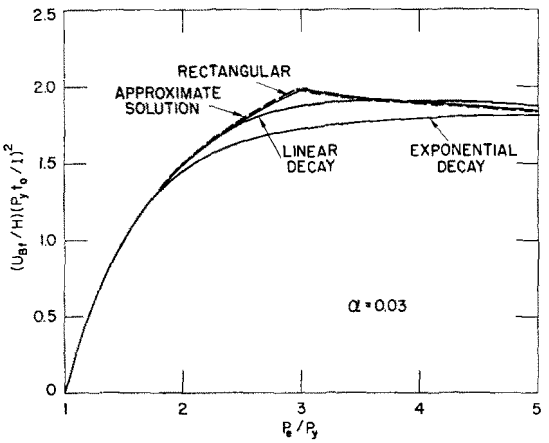

Fig. 12. Final mid-span deflection in small deformation range as function of effective pressure for various pulse shapes.

respectively, for various pulse shapes, where P_m is the peak pressure of the pulse and P_e is its effective value as computed from equations (43). The exponential decay and rectangular pulses are defined by equations (40) and (41), and the linear decay pulse is defined by

$$P(t) = P_m\left(1 - \frac{t}{t_2}\right), \qquad 0 \le t \le t_2$$
$$P(t) = 0, \qquad t < 0 \quad \text{and} \quad t > t_2 . \tag{46}$$

The time constants for the various pulses are chosen small enough that the response is in the small deformation range.

From Fig. 11 we see that the final deflection is strongly dependent on the pulse shape, even for pulses which have the same peak value and impulse. At $P_m = 2P_y$, for example, the deformation produced by a rectangular pulse is roughly twice that produced by an exponential-decay pulse. Considering the same deformations as functions of the effective pressure,

as in Fig. 12, compresses the curves together. The dashed line in Fig. 12 is for an approximate closed-form solution for small deformation response given in Appendix A.

In order to obtain a prediction for t_f analogous to that of equation (45), $t_f P_y/I$ is plotted as a function of P_e/P_y in Fig. 13 for various pulse shapes†. We see that $t_f P_y/I$ is close to unity for a range of values of P_e/P_y and also that the curve for the approximate solution is a reasonable representation for the other curves.

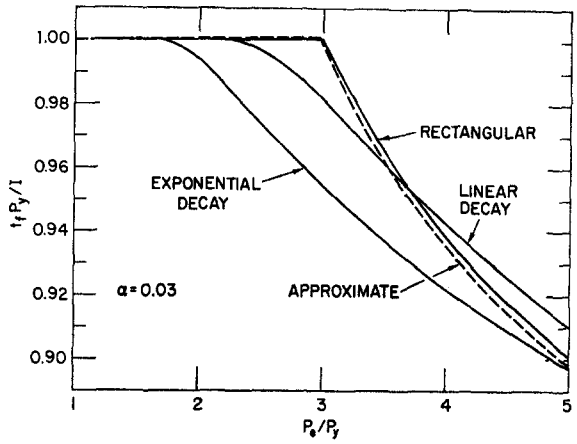

Fig. 13. Response duration as function of effective pressure for small deformation range.

Large deformation response

Because of membrane effects, an internally pressurized hexagon deforms into a shape which can statically withstand a pressure higher than the initial yield load. This static large-deformation solution is derived in Appendix B. Applying a step pulse results in a large deformation dynamic plastic response which stops at some time t_f dependent on the pulse height and the geometric parameter α. Consequently the response to a rectangular pulse with duration greater than t_f is identical to the response to a step pulse with the same height. Results will be shown next for the final plastic deformations and response times produced by step pulses.

Consider a step pulse defined by

$$\begin{aligned} P(t) &= P_m, \qquad 0 \le t < \infty, \\ P(t) &= 0, \qquad t < 0. \end{aligned} \tag{47}$$

The final plastic deformation at the mid-point of a side divided by the wall thickness is given in Fig. 14 as a function of the ratio of step pulse height to limit load for various values of α. It is apparent from the curves that a thin hexagon must deform relatively more than a thick one in order to contain a given multiple of its respective yield load. The final displacement of a corner divided by the wall thickness is shown in Fig. 15 as a function of P_m/P_y for various values of α. Except for thick walls and small step pulse height to yield load ratios, U_{Af} is negative, i.e. the corners of the hexagon more inwards in response to the step pulse. The ratio of response time t_f to time constant t_0 (see equations 1) is plotted in Fig. 16 as a function of step pulse height divided by limit load for various values of α.

† $t_y = 0$ for the pulses shown.

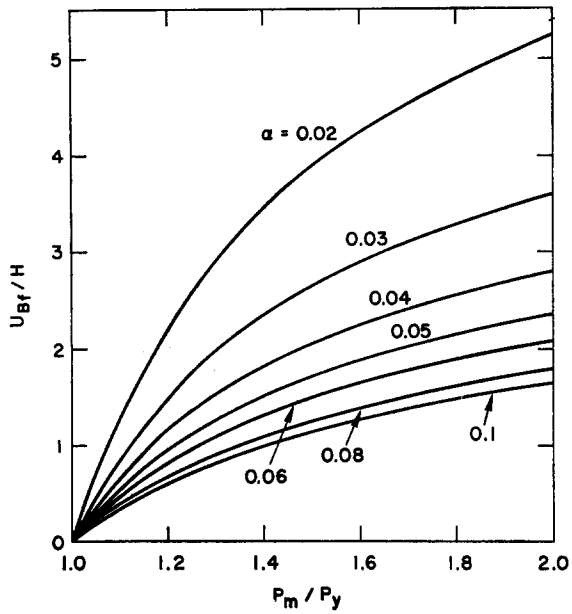

Fig. 14. Final mid-span deflection for large deformation response to a step pulse.

Parameter studies were performed to determine the effect of pulse shape on the large deformation response of the hexagon[7]. Some typical results will be presented here, and the permanent plastic deformation produced by an arbitrary pulse will be related to that produced by an equivalent step pulse.

Figure 17 shows results for an exponential decay pulse, defined by equation (40), with $\alpha = 0{\cdot}056$. Computations were made for various combinations of the pulse parameters P_m and t_1. The peak pressures chosen were $P_m = 0{\cdot}26P_0, 0{\cdot}3P_0, 0{\cdot}35P_0, 0{\cdot}4P_0, 0{\cdot}45P_0, 0{\cdot}5P_0$, and $0{\cdot}55P_0$; for each of these values of P_m, calculations were performed for $t_1 = t_0, 2t_0, 3t_0, 4t_0$, and $5t_0$. The characteristic time constant t_0 for the plastic response is defined by equations (1), and P_0 is the limit load of the circumscribed circular ring, given by

$$P_0 = \sigma_y \frac{H}{L}. \tag{48}$$

The open circles on Fig. 17 are the values of U_{Bf}/H plotted as a function of P_m/P_0, and the solid circles are the same values of U_{Bf}/H plotted as a function of P_{AVG}/P_0, where P_{AVG} is the average pressure applied during the plastic response, i.e.

$$P_{AVG} = \frac{1}{t_f}\int_0^{t_f} P(t)\,dt. \tag{49}$$

The curve on the figure is the permanent deformation produced by a step pulse of height P_m. It is apparent that a step pulse and an exponential-decay pulse which have the same average value during the response produce essentially the same permanent plastic deformation.

Similar results are shown in Fig. 18 for linear-decay pulses (see equation 46) with $\alpha = 0{\cdot}056$. Again the permanent plastic deformation is a function of the average pressure applied during the deformation. This functional relationship is known from the step pulse results.

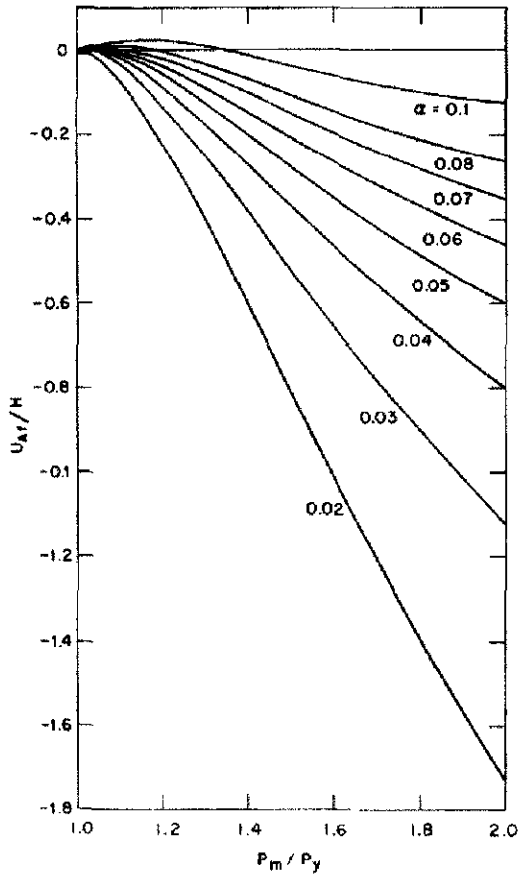

Fig. 15. Final corner deflection for large deformation response to a step pulse.

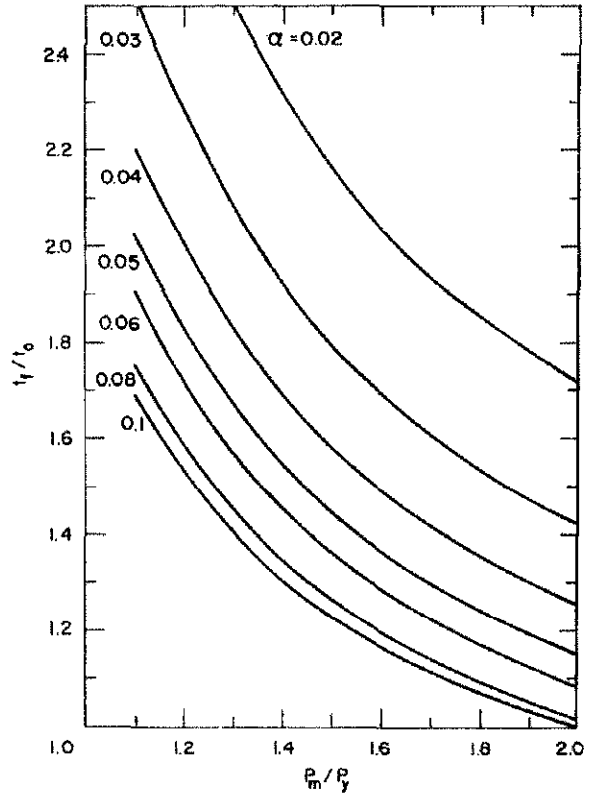

Fig. 16. Response duration as function of step pulse height.

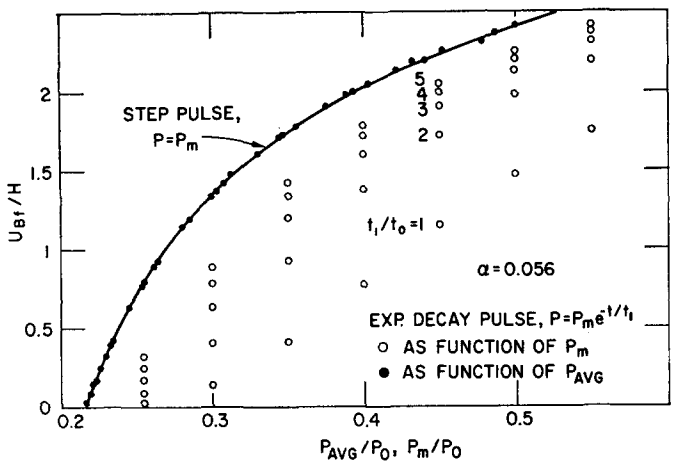

Fig. 17. Comparison of results in the large deformation range for exponential-decay and step pulses.

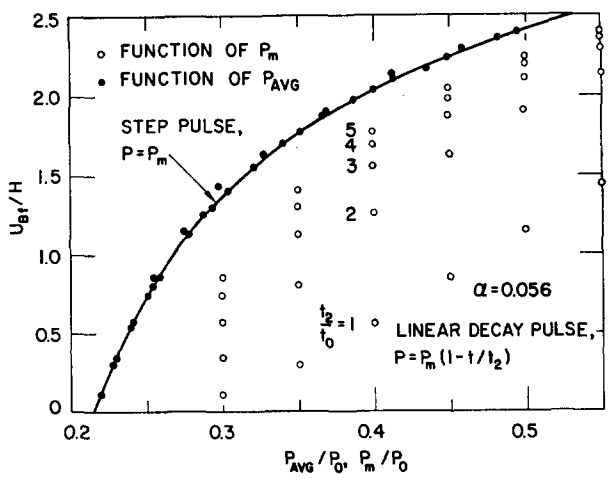

Fig. 18. Comparison of results in the large deformation range for linear-decay and step pulses.

In experiments where $U_B(t)$, $P(t)$, U_{Bf}, and t_f can be measured, P_{AVG} is easily determined from P and t_f and the correlation of U_{Bf} to P_{AVG} can be investigated. For analytical studies, however, there appears to be no simple relationship analogous to equations (45) for the small deformation range to predict t_f for the large deformation response. Without an *a priori* determination of t_f for a given pulse either the response to the step pulse with the same height as the peak (rather than the average) pressure of the pulse may be used to bound the permanent deformation, or the computer solution may be obtained for the given pulse.

CONCLUSIONS

The permanent plastic deformation of a hexagon resulting from a pressure pulse has been shown to be dependent on the pulse shape, magnitude, and duration. The nature of this dependence is qualitatively different in the small and large deformation ranges.

The correlation of permanent plastic deformation to pulse parameters in the small deformation range implies that an earlier occurring peak produces more deformation than a later one of the same height and impulse. This is because an earlier peak results in a smaller value of the moment arm of the pressure shape, t_m, and, consequently, in a larger value of the effective pressure, P_e. The response time in the small deformation range is proportional to the time scale of the pulse and is independent of the material and geometric constants of the hexagon.

In the large deformation range the permanent plastic deformation depends on the average pressure applied during the deformation and, therefore, is not sensitive to the location of the peak pressure. The characteristic response time is virtually independent of the pulse time-scale for long duration pulses but depends on the material and geometric constants of the hexagon through α, t_0, and P_y. This response time is of the same order of magnitude as the pulse durations to which a reactor subassembly may be exposed.

REFERENCES

1. C. K. Youngdahl, Correlation parameters for eliminating the effect of pulse shape on dynamic plastic deformation, *J. appl. Mech.* **39**, 744 (1970).
2. P. S. Symonds and T. J. Mentel, Impulsive loading of plastic beams with axial constraints, *J. Mech. Phys. Solids* **6**, 186 (1958).
3. N. Jones, Influence of strain-hardening and strain-rate sensitivity on the permanent deformation of impulsively loaded rigid-plastic beams, *Int. J. Mech. Sci.* **9**, 777 (1967).
4. P. S. Symonds and N. Jones, Impulsive loading of fully clamped beams with finite plastic deflections and strain-rate sensitivity, *Int. J. Mech. Sci.* **14**, 49 (1972).
5. W. Prager, *An Introduction to Plasticity*. Addison-Wesley (1959).
6. N. W. Clark, DIFSUB, 3600 FORTRAN subroutine which performs one integration step for a system of first order ordinary differential equations. *ANL Library Subroutine ANL-D250* (1966).
7. C. K. Youngdahl, *Parameter studies on the effect of pulse shape on the dynamic plastic deformation of a hexagon*. Argonne Nat. Lab. Rep. ANL-8012 (1973).
8. C. K. Youngdahl and G. S. Rosenberg, Dynamic load factors for plastic deformation of hexagonal subassembly ducts. *Nucl. Eng. and Design* **24**, 105 (1973).

APPENDIX A. APPROXIMATE SMALL-DEFORMATION SOLUTION

Many terms in the governing sets of differential equations are negligible if the pulse duration is such that the displacements of the sides of the hexagon are small compared to its wall thickness. An approximate, closed-form solution can then be obtained for rectangular pulses. This approximate solution is useful because pulses of other shapes are equivalent to rectangular pulses in producing final plastic deformation if the effective pressures and impulses are the same. The following approximations can reasonably be made if the deformation is small:

$$\theta \simeq 0, \quad N_A \simeq N_B, \quad V_T \simeq 0, \quad U_A \simeq 0, \quad \Delta_A \ll L, \quad \Delta_B \ll L,$$
$$\frac{d\Delta_A}{dt} \simeq 0, \quad \frac{d\Delta_B}{dt} \simeq 0. \tag{A.1}$$

The response to the initial jump of a rectangular pulse, equations (41), can be in either the first or second deformation modes, depending on the magnitude of P_r.

Initial first mode response

Making the approximations in the governing equations for first mode response results in the following sets of approximate equations:

$$\begin{aligned} V_P^* - \frac{L}{4}\Omega^* &= 0, \\ \frac{\rho H L^3}{96}\frac{\mathrm{d}\Omega^*}{\mathrm{d}t} &= -2M_B^* + \frac{N_B^* L}{4\sqrt{3}}, \\ \frac{\rho H L}{2}\frac{\mathrm{d}V_P^*}{\mathrm{d}t} &= \frac{PL}{2} - \frac{N_B^*}{\sqrt{3}}, \\ M_B^* = M_A^* &= M_0\left[1 - \left(\frac{N_B^*}{N_0}\right)^2\right], \\ \frac{\mathrm{d}\theta^*}{\mathrm{d}t} &= \Omega^*, \\ U_B^* &= \frac{L}{2}\theta^*. \end{aligned} \tag{A.2}$$

The asterisks indicate that the solution is an approximation to the numerical solution of the "exact" set of differential equations.

For a rectangular pulse, the solution in the interval $0 \le t \le t_r$ gives

$$U_B^* = \frac{Hf_1 t^2}{t_0^2}, \tag{A.3}$$

where

$$f_1 = \frac{P_r}{\alpha^2\sigma_y} = \frac{2}{9\alpha^2}\left(\sqrt{1 + 27\alpha^2 + \frac{9P_r}{4\sigma_y}} - 1\right). \tag{A.4}$$

The solution for U_B^* for the remainder of the motion $t_r \le t \le t_f$ is

$$U_B^* = \frac{H}{t_0^2}[-f_2(t - t_r)^2 + 2f_1 t_r(t - t_r) + f_1 t_r^2], \tag{A.5}$$

where

$$f_2 = \frac{6}{1 + \sqrt{1 + 27\alpha^2}}. \tag{A.6}$$

The time t_f^* when the deformation stops is when $V_P^* = 0$. It is given by

$$t_f^* = t_r\left(1 + \frac{f_1}{f_2}\right). \tag{A.7}$$

Substituting this result into equation (A.5) gives

$$U_B^*(t_f^*) = \frac{Hf_1 t_r^2}{t_0^2}\left(1 + \frac{f_1}{f_2}\right) \tag{A.8}$$

for the final plastic deformation at mid-span. As $\alpha \to 0$,

$$U_B^*(t_f^*) \to 3H\left(\frac{P_r t_r}{P_y t_0}\right)^2\left(1 - \frac{P_y}{P_r}\right). \tag{A.9}$$

Initial second mode response

The use of the approximations of equations (A.1) in the governing equations for second mode response results in the following set of approximate equations:

$$V_P^* - \frac{L}{4}(1-\varepsilon^*)\Omega^* = 0,$$

$$V_\varepsilon^* = 2V_P^*,$$

$$\rho H V_B^* = \int P\,\mathrm{d}t + G^*(0),$$

$$\rho H V_\varepsilon^* = \int P\,\mathrm{d}t + G^*\left(\frac{\varepsilon^* L}{2}\right),$$

$$\frac{\rho H L^3}{96}(1-\varepsilon^*)^3\frac{\mathrm{d}\Omega^*}{\mathrm{d}t} = -2M_B^* + \frac{N_B^* L}{4\sqrt{3}}(1-\varepsilon^*),$$

$$\frac{\rho H L}{2}(1-\varepsilon^*)\frac{\mathrm{d}V_P^*}{\mathrm{d}t} = \frac{PL}{2}(1-\varepsilon^*) - \frac{N_B^*}{\sqrt{3}},$$

$$M_B^* = M_A^* = M_0\left[1-\left(\frac{N_B^*}{N_0}\right)^2\right],$$

$$\frac{\mathrm{d}\theta^*}{\mathrm{d}t} = \Omega^*,$$

$$\frac{\mathrm{d}U_B^*}{\mathrm{d}t} = V_B^*. \tag{A.10}$$

For $\frac{\mathrm{d}\varepsilon^*}{\mathrm{d}t} \geq 0$, the approximate hinge-band growth equation is

$$12\sqrt{3}\,M_B^* - N_B^* L(1-\varepsilon^*) = 0. \tag{A.11}$$

Assuming P_r is large enough that second mode response is initiated, the hinge band has a constant width ε_0^* in the interval $0 \leq t \leq t_r$. The solution in this interval results in

$$\begin{aligned} \varepsilon^* = \varepsilon_0^* &= 1 - \frac{4\alpha\sigma_y N_B^*}{\sqrt{3}\,P_r N_0}, \\ U_B^* &= \frac{HP_r t^2}{2\alpha^2\sigma_y t_0^2}. \end{aligned} \tag{A.12}$$

The approximate transition pressure P_h^* between initial first and second mode response to an instantaneous jump is the value of P_r for which $\varepsilon_0^* = 0$. From equations (A.12), P_h^* is given by

$$P_h^* = \frac{24\alpha^2\sigma_y}{1+\sqrt{1+108\alpha^2}}. \tag{A.13}$$

After the end of the pulse, the second mode response continues as ε decreases from ε_0 to zero. Let t_ε^* be the time at which the second mode response ends. The solution to equations (A.10) in the interval $t_r \le t \le t_\varepsilon^*$ is, using the continuity conditions on the velocities and displacements at t_r,

$$1 - \varepsilon^* = \left[(1 - \varepsilon_0^*) + \frac{48\alpha^2\sigma_y}{P_r}\left(\frac{t}{t_r} - 1\right)\right]^{1/2},$$
$$U_B^* = \frac{HP_r t_r(2t - t_r)}{2\alpha^2\sigma_y t_0^2}. \tag{A.14}$$

The time when the second mode response ends is given by

$$t_\varepsilon^* = t_r\left[1 + \frac{P_r}{48\alpha^2\sigma_y} - \frac{\sigma_y}{4\sigma_y + 9P_r}\right]. \tag{A.15}$$

In the interval $t_\varepsilon^* \le t \le t_f$, the motion is in the first deformation mode so that equations (A.2) apply (except for the equation for U_B^*, which is found from $\frac{U_B^*}{\mathrm{dt}} = V_B^*$). Applying the continuity conditions on the velocities and displacements at t_ε^*, the solution in this interval is

$$U_B^* = \frac{H}{t_0^2}\left[-f_2(t - t_\varepsilon^*)^2 + \frac{P_r t_r}{\alpha^2\sigma_y}(t - t_\varepsilon^*)\right] + U_B^*\Big|_{t_\varepsilon^*}. \tag{A.16}$$

The time t_f^* when the motion stops is found from $V_P^*(t_f^*) = 0$; it is given by

$$t_f^* = t_\varepsilon^* + \frac{P_r t_r}{2\alpha^2\sigma_y f_2}. \tag{A.17}$$

The final plastic deformation at the mid-point of a side is then

$$U_B^*(t_f^*) = \frac{HP_r^2 t_r^2}{4\alpha^4\sigma_y^2 t_0^2 f_2} + U_B^*\Big|_{t_\varepsilon^*}, \tag{A.18}$$

where U_B^* at t_ε^* is computed from equation A.14. As $\alpha \to 0$,

$$U_B^*(t_f^*) \to H\left(\frac{P_r t_r}{P_y t_0}\right)^2\left(\frac{5}{3} + \frac{P_y}{P_r}\right). \tag{A.19}$$

The final deformation results for the deformation at mid-span are computed from equations (A.8) and (A.18) and plotted in Fig. 19, in the nondimensional form $U_B^*(t_f^*)t_0^2/Ht_r^2$, as a function of P_r/σ_y for $\alpha = 0{\cdot}056$. Also shown are the corresponding results for the numerical solution of the "exact" equations with $t_r = 0{\cdot}01t_0$.

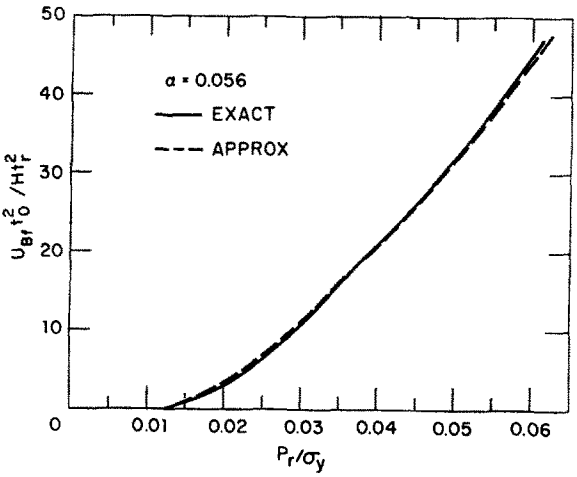

Fig. 19. Comparison of exact and approximate solutions for small deformation response to rectangular pulses.

From these results and other computations, it is apparent that the approximate solution for rectangular pulses is a good match in the small deformation range to the numerical solution of the exact equations.

APPENDIX B. STATIC LARGE DEFORMATION SOLUTION

The acceleration terms in the equations of motion vanish for a static pressure P_s. From the equations of motion for the first mode (equation 12) and the yield condition (equation 13), we then have

$$\begin{aligned} &4M_0\left[2-\left(\frac{N_A}{N_0}\right)^2-\left(\frac{N_B}{N_0}\right)^2\right]+N_B L\sin\theta+N_A L\left(\sin\theta-\frac{\cos\theta}{\sqrt{3}}\right)=0,\\ &P_s L-2N_B\sin\theta+2N_A\left(\frac{\cos\theta}{\sqrt{3}}-\sin\theta\right)=0,\\ &N_A\left(\cos\theta+\frac{\sin\theta}{\sqrt{3}}\right)-N_B\cos\theta=0. \end{aligned} \tag{B.1}$$

The solution for N_A and N_B in terms of θ and P_s is

$$\begin{aligned} N_A&=\frac{\sqrt{3}}{2}P_s L\cos\theta,\\ N_B&=\frac{1}{2}P_s L(\sqrt{3}\cos\theta+\sin\theta), \end{aligned} \tag{B.2}$$

and the resulting quadratic relationship between P_s and $\tan\theta$ is

$$(8\alpha^2\sigma_y^2+2\sigma_y P_s-P_s^2)\tan^2\theta+2\sqrt{3}P_s(2\sigma_y-P_s)\tan\theta+8\alpha^2\sigma_y^2-2\sigma_y P_s-6P_s^2=0. \tag{B.3}$$

Note from equations (8) and (B.3) that $P_s=P_y$ at $\theta=0$, which agrees with the limit-load analysis.

The plastic stretch in the half-side must be determined in order to compute the static corner and midspan deflections. From the flow rules given in equation (13), we have that

$$\frac{d(\Delta_A + \Delta_B)}{d\theta} = \frac{N_A + N_B}{2\sigma_y}, \tag{B.4}$$

or, using equation (B.2),

$$\frac{d(\Delta_A + \Delta_B)}{d\theta} = \frac{P_s L}{4\sigma_y}(2\sqrt{3}\cos\theta + \sin\theta). \tag{B.5}$$

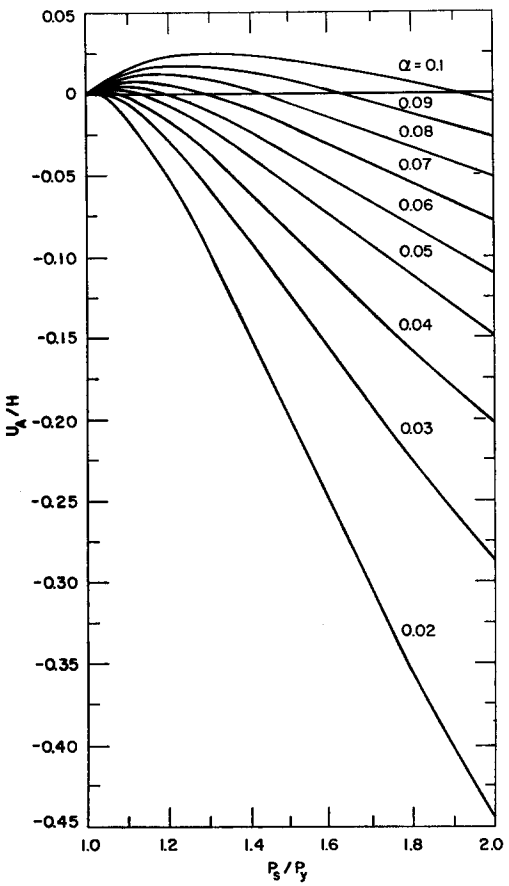

Fig. 20. Corner deflection as function of static pressure.

Since P_s is known from equation (B.3) as a function of θ, equation (B.5) is easily integrated numerically. The deflections U_A and U_B are then found from equation (15); the results are shown in Figs. 20 and 21 for various values of α. We see that the static deflection at the corner may be either inward or outward, depending on the combination of α and P_s/P_y.

The substitution of equation (B.2) into equation (17) gives

$$\frac{\partial^2 M}{\partial x^2} = -P_s, \tag{B.6}$$

so that the bending movement always has a relative maximum at $x = 0$. Consequently, the second deformation mode cannot occur for a static load.

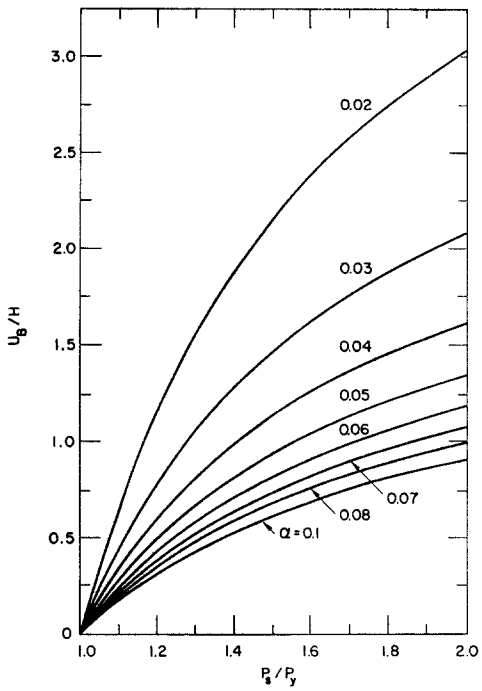

Fig. 21. Mid-span deflection as function of static pressure.

These results are valid for $P_s \geq P_y$ and $N_B < N_0$. At the corner of the yield condition corresponding to $N = N_0$, the direction of the strain rate vector is indeterminant and equation (B.4) cannot be used.

Абстракт — Исследуется динамическое пластическое поведение шестиугольной рамы, подверженной действию внутренного импульса давления произвольного очертания, учитывая геометрическое эффекты больших деформаций, которые происходят в повторном распределении реакций от изгиба и мембранных усилий. Рассматриваются максимальные значения давлений для несколько многократных чисел для статической нагрузки течения. Принимается материал рамы как жесткий, идеально пластический. Определяется эффект очертания импульса на окончательную пластическую деформацию путем численного решения системы дифференциальных уравнений состояния, для разнообразия комбинаций параметров. В области малых деформаций указано, что остаточная пластическая деформация зависит от эффективного давления, определенного членами первого момента импульса давления. Длительность реагирования пропорциональна к длительности импульса. В области больших деформаций остаточная пластическая деформация является функцией среднего давления, приложенного во время реагирования. Длительность реагирования зависим от постоянной характеристического времени, которая является функцией свойств материала и шестиугольного очертания.